Journal of Applied Physics

RESEARCH ARTICLE | JULY 11 2024

Thermal relaxation of strain and twist in ferroelectric hexagonal boron nitride moiré interfaces

Special Collection: Two-Dimensional Materials and Heterostructures Under Strain

Marisa Hocking ; Christina E. Henzinger ; Steven J. Tran ; Mihir Pendharkar ; Nathan J. Bittner; Kenji Watanabe ; Takashi Taniguchi ; David Goldhaber-Gordon ; Andrew J. Mannix

J. Appl. Phys. 136, 024303 (2024)
https://doi.org/10.1063/5.0210112

Journal of Applied Physics ARTICLE pubs.aip.org/aip/jap

Thermal relaxation of strain and twist in ferroelectric hexagonal boron nitride moiré interfaces

Cite as: J. Appl. Phys. **136**, 024303 (2024); doi: 10.1063/5.0210112
Submitted: 25 March 2024 · Accepted: 8 June 2024 ·
Published Online: 11 July 2024

Marisa Hocking,[1,2] Christina E. Henzinger,[1] Steven J. Tran,[2,3] Mihir Pendharkar,[1,2] Nathan J. Bittner,[4] Kenji Watanabe,[5] Takashi Taniguchi,[6] David Goldhaber-Gordon,[2,3] and Andrew J. Mannix[1,2,a)]

AFFILIATIONS

[1]Department of Materials Science and Engineering, Stanford University, Stanford, CA 94305
[2]Stanford Institute for Materials and Energy Sciences, SLAC National Accelerator Laboratory, Menlo Park, CA 94025, USA
[3]Department of Physics, Stanford University, Stanford, CA 94305, USA
[4]Minneapolis, Minnesota 55419, USA
[5]Research Center for Electronic and Optical Materials, National Institute for Materials Science, 1-1 Namiki, Tsukuba 305-0044, Japan
[6]Research Center for Materials Nanoarchitectonics, National Institute for Materials Science, 1-1 Namiki, Tsukuba 305-0044, Japan

Note: This paper is part of the special topic, Two-Dimensional Materials and Heterostructures Under Strain.

[a)]**Author to whom correspondence should be addressed:** ajmannix@stanford.edu

ABSTRACT

New properties can arise at van der Waals (vdW) interfaces hosting a moiré pattern generated by interlayer twist and strain. However, achieving precise control of interlayer twist/strain remains an ongoing challenge in vdW heterostructure assembly, and even subtle variation in these structural parameters can create significant changes in the moiré period and emergent properties. Characterizing the rate of interlayer twist/strain relaxation during thermal annealing is critical to establish a thermal budget for vdW heterostructure construction and may provide a route to improve the homogeneity of the interface or to control its final state. Here, we characterize the spatial and temporal dependence of interfacial twist and strain relaxation in marginally-twisted hBN/hBN interfaces heated under conditions relevant to vdW heterostructure assembly and typical sample annealing. We find that the ferroelectric hBN/hBN moiré at very small twist angles ($\theta \leq 0.1°$) relaxes minimally during annealing in air at typical assembly temperatures of 170°C. However, at 400°C, twist angle relaxes significantly, accompanied by a decrease in spatial uniformity. Uniaxial heterostrain initially increases and then decreases over time, becoming increasingly non-uniform in direction. Structural irregularities such as step edges, contamination bubbles, or contact with the underlying substrate result in local inhomogeneity in the rate of relaxation.

I. INTRODUCTION

The weak van der Waals bonding between layers of 2D materials such as graphene and hexagonal boron nitride (hBN) facilitates the assembly of heterostructures. For interfaces between two layers, a twist angle or small difference in lattice constant will result in a moiré superlattice. This decoupling from the atomic lattice permits the fabrication of unprecedented structures that can exhibit phenomena including unconventional superconductivity,[1] orbital ferromagnetism,[2] and Wigner states.[3]

In monolayers that lack inversion symmetry, such as WSe_2,[4,5] MoS_2,[5,6] and hBN,[7–9] out-of-plane ferroelectricity emerges for stacking sequences which break inversion symmetry. For perfect rotational alignment between layers, this generates a single ferroelectric domain. In practice, targeting zero twist when assembling a vdW stack produces a finite near-zero twist—"marginally twisted" regime "resulting in a moiré lattice which relaxes into ferroelectric domains (two per moiré unit cell, with one polarity upward and one polarity downward).[6,8,9] The domain boundaries—variously

referred to as soliton domain boundaries or partial dislocations—will form a perfect dislocation upon meeting and can only be eliminated by reaching an edge of the sample.[4] Applying an out-of-plane electric field causes the ferroelectric domains with polarity aligned along the applied field to expand and anti-aligned domains to contract via bowing of the domain walls, but complete nucleation or annihilation of an individual domain is difficult.[4,6]

Previous works have used the spatial modulation of electrostatic potential in ferroelectric hBN to modify the opto-electronic properties of an adjacent 2D semiconductor (i.e., a "proximity moiré" effect), revealing distinct excitonic species in regions with opposite polarization[10] as well as confining exciton diffusion lengths.[11] However, characterizing the optical excitations associated with a single domain requires individual domains that are optically addressable, i.e., at least several hundred nanometers wide. This necessitates achieving twist angles within a few tenths of a degree from zero (e.g., $< 0.03°$ for domains to reach > 500 nm). Current heterostructure assembly techniques cannot reliably reach this small angle, typically deviating from the intended angle due to twist relaxation and unintentional mechanical forces during assembly. Post-assembly modification of moiré superlattices is an appealing alternative route to increase yield of samples with large domains of alternating polarizations and potentially as a general processing route for any heterostructure with a larger-than-intended twist.

The interface between two incommensurate flakes may display superlubricity—easy slippage with respect to each other.[12] Thus, applying mechanical force after stacking has succeeded in producing macroscopic rotation.[12–16] However, interfaces nearing commensurability (as at the low twist angles we have described targeting) may be locked into place,[12] preventing further rotation without damaging the material. Another limitation is that applying forces to drive rotation has typically involved contacting the sample with an external probe, which may increase contamination on the surface or deform the flakes.

High-temperature annealing after assembly has been shown to alter interfacial twist.[14,17,18] Previous experimental efforts have shown that there is a maximum critical angle ($\theta_c > 1°$) below which the interface relaxes toward 0°[14,18] as well as a critical temperature ($T_c \geq 600$°C) at which incommensurate regions begin moving or are entirely driven out.[18–22] Relaxation below T_c has been less frequently studied with results ranging from a linear reduction in twist angle[14] to local fluctuation of an incommensurate domain wall without macroscopic rotational relaxation.[23] Reports suggest that the interfacial twist becomes more (less) uniform for heterostructures with large (small) initial angles after annealing below T_c,[21,24] though this is commonly extracted from fingerprint Raman peaks, which is an optical technique with a spot size on the order of several hundred nanometers. Moreover, the effect of annealing on strain, which heavily influences the geometry of the moiré as well as electronic behavior, is not well understood.

Here, we study the effects of thermal annealing upon marginally twisted ferroelectric hBN/hBN interfaces. We create a series of twisted hBN samples with angles $\leq 0.3°$. They are annealed at elevated temperatures in both air and vacuum for sustained periods of time. Before and after annealing, the real-space moiré is mapped using scanning probe techniques. We extract the nominal interlayer twist and uniaxial heterostrain within each region by applying real-space and reciprocal-scape analysis techniques. At 400°C, we find a reduction in twist that saturates at longer annealing times. Uniaxial heterostrain typically increases but then reduces again. These changes are spatially inhomogeneous and are sensitive to structural irregularities such as step edges or contact with the underlying substrate. Our work provides an estimate of the thermal budget for controlled annealing of ferroelectric structures.

II. RESULTS

A. Extracting twist and strain

The lowest-energy structure for bulk hBN exhibits an AA" stacking conformation, shown in Fig. 1(a). Monolayer hBN lacks inversion symmetry due to the distinct B and N sublattices. In the AA" stacking arrangement, the top layer is effectively rotated 60° (or equivalently, 180°) with respect to the bottom layer, which creates an inversion center at the interface. In antiparallel stacking, which mimics the bulk-like AA" stacking with a small lateral displacement in the upper layer, the lattice will reconstruct to form primarily commensurate AA" domains bounded by regions of energetically unfavorable AB" stacking and incommensurate domain walls, shown in Fig. 1(d). The antiparallel configuration seen in Fig. 1(b) is not ferroelectric as it maintains inversion symmetry. However, in parallel stacking, the lattice reconstructs to the energetically favorable AB (BA) arrangement shown in Fig. 1(c). The AB and BA domains are separated by small regions of AA stacking and incommensurate domain walls as seen in Fig. 1(e). The parallel stacking configuration lacks inversion symmetry, allowing spontaneous polarization through a dipole moment from the distorted orbital of the nitrogen atom.[8]

These reconstructions occur because the system seeks to minimize stacking fault energy by reducing the area of incommensurate regions at the competing energetic cost of mutual lattice adjustment (i.e., longitudinal and torsional strain). As the relative twist angle θ between the two layers approaches 0°, small amounts of uniaxial heterostrain ϵ introduce anisotropy into the reconstruction. The visual effect of strain on a lattice scales inversely with the twist angle ($\propto 1/\theta$), which can magnify the effects of strain variation in marginally twisted structures.[25]

The real-space domains and domain boundaries can be imaged using scanning probe techniques, which are sensitive to the contrast in mechanical or electrical properties between the distinct regions produced by the reconstruction. These may include piezoresponse force microscopy (PFM),[8,26] Kelvin probe force microscopy (KPFM),[7,9] contact resonance atomic force microscopy (CR-AFM),[27,28] and other modes to measure nanomechanical response.[29] For many techniques measuring variation in mechanical properties, the phase (or frequency, if using a phase-locked loop) channel is most sensitive to these deviations.[27,30] While the topography for these samples only shows morphological defects as in Fig. 1(f), the CR-AFM phase channel [Fig. 1(g)] shows the domain walls of a ferroelectric reconstruction. Thermal annealing significantly alters the geometry of the reconstruction by enlarging and—in some cases—elongating the domains in Fig. 1(h).

Extracting twist and strain from real-space moiré lattices can be difficult, particularly from non-uniform or small twist angle moirés. Commonly, real-space images are converted to a frequency-space

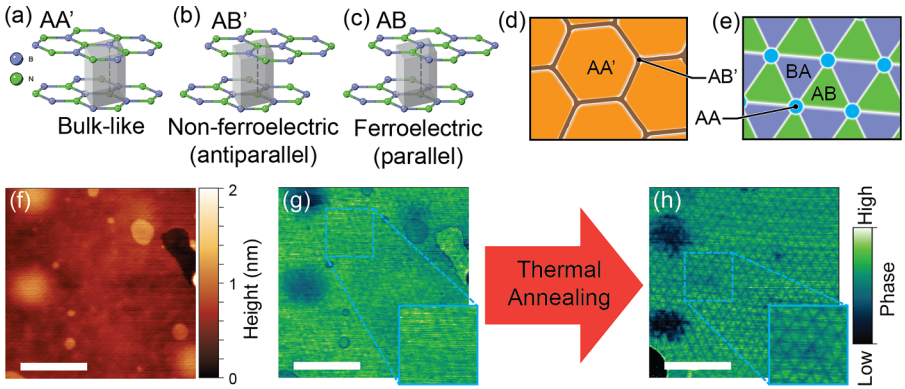

FIG. 1. Crystallographic arrangement of hBN in its (a) bulk-like state as well as its (b) antiparallel and (c) parallel stacking configuration. After stacking, the moiré can relax into either (d) a bulk-like reconstruction with small AB" regions or (c) a triangular reconstruction with oppositely polarized AB/BA domains, which is the ferroelectric reconstruction. In a ferroelectric hBN sample measured using contact resonance AFM (CR-AFM), the topography shows only morphological defects (f), while the phase channel shows the real-space moiré domains (g). These domains can be altered by thermal annealing as seen in the phase channel of the same region after treatment (h). All scale bars are 500 nm.

representation via a fast Fourier transform (FFT), enabling the extraction of three reciprocal lattice vectors. In the limit of small deformations, assuming that biaxial strain and homostrain are negligible, these vectors can be fit to determine the wavelengths for a superlattice with small interfacial twist θ and uniaxial heterostrain with magnitude ϵ and direction ϕ,[31]

$$\mathbf{g}_{i=1,2} = \mathcal{E}^{\top}\mathbf{G}_{i=1,2}, \tag{1}$$

$$\mathcal{E} \equiv \mathcal{T}(\theta) + \mathcal{S}(\epsilon, \phi), \tag{2}$$

$$\mathcal{T} = \begin{pmatrix} 0 & -\theta \\ \theta & 0 \end{pmatrix}, \mathcal{S}(\epsilon, \phi) = R_{\phi}^{\top}\begin{pmatrix} -\epsilon & 0 \\ 0 & \nu\epsilon \end{pmatrix}R_{\phi}, \tag{3}$$

where $\mathbf{g}_i$ and $\mathbf{G}_i$ are the moiré and undeformed reciprocal space lattice vectors for lattice vector i, $\mathcal{E}$ is the deformation lattice, $\mathcal{T}$ describes the deformation of the lattice due to twist, $\mathcal{S}$ describes the deformation of the lattice due to strain, R_{ϕ} is the two-dimensional rotation matrix using the shear angle ϕ, and ν is Poisson's ratio $\approx$ 0.21.[32]

Following this set of equations, increasing the interfacial twist decreases the average size of the moiré domain, whereas strain contributes to the anisotropy of the domain in a direction determined by the shear angle. At low twist angles, the individual layers' lattices relax so that the majority of each domain is commensurate. However, we retain a value of θ to facilitate comparison to other works.

For moirés in which the periodicity is consistent throughout the field of view, as in Fig. 2(a), an FFT-based twist and strain extraction method can extract accurately representative values. However, in cases where the twist and/or strain exhibits only a few spatial periods or is heterogeneous within the imaged region, the moiré lacks long-range order needed to generate a strong peak in frequency space, and the FFT is weak or distorted as in Fig. 2(b).

For these cases in which the frequency-space method is unsuitable, a real-space representation can provide complementary and precise representation of the moiré. The real-space moiré is extracted through identification of the individual moiré domains, by either automated methods[20,33] or by careful manual tracing of the domain boundaries[34] as in Fig. 2(c). Each node and its six nearest neighbors can be found, and the real-space moiré lattice wavelengths λ_1, λ_2, and λ_3 can then be measured (neglecting curvature of the domain walls) for each individual triangle which comprises the relaxed half-moiré unit cell. Under the assumption that strain is purely uniaxial heterostrain, the per-triangle wavelengths can be transformed to reciprocal space and fit to Eqs. (1)–(3). For relatively uniform regions as in Fig. 2(a), the real-space fit and the FFT fit show comparable results with respect to twist angle and strain, seen in Fig. 2(d), although the real-space fit gives a more complete representation of the distribution. For regions with stronger variation as in Fig. 2(b), the FFT has increasingly spread out and less intense peaks, so the moiré cannot be well-described by a single peak in frequency space, as seen in Fig. 2(e).

B. Temperature- and time-dependence of relaxation

Studies have shown complete relaxation toward 0° of ferroelectric transition-metal dichalcogenide (TMDC) heterostructures assembled at an arbitrary angle upon heating to above 800°C,[18] suggesting that full relaxation is possible for other 2D ferroelectric structures, but the associated relaxation dynamics have not been characterized. To address this, we annealed ferroelectric hBN samples under conditions typical of assembly and sample processing. To mimic sample assembly in air, hBN/hBN samples were annealed on a hot plate in air for discrete time steps, then the moirés were measured at room temperature using PFM or CR-AFM in roughly the same position indicated in Figs. 3(a) and 3(f) each time. We employed PFM before the utility of CR-AFM was realized, but the techniques are equivalent as they are both able to extract the spatial

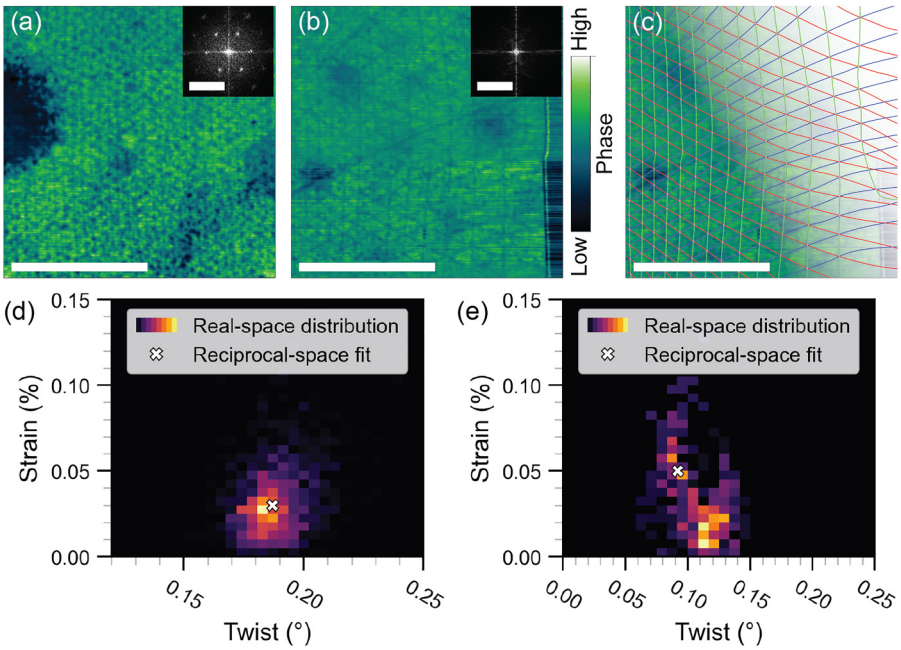

FIG. 2. Analysis methods for near-zero twisted superlattices. The CR-AFM phase and related inset FFT are shown in (a) for a small, uniform moiré and (b) for a larger, non-uniform moiré. The domain walls of these near-zero twist superlattices can be manually traced in a vector program with an example seen in (c), and the twist and strain are computed on a per-triangle basis. For the uniform moiré from (a), the triangle-wise distribution (real-space distribution) of twist and strain is consistent with the peak twist and strain calculated directly from the FFT (reciprocal-space fit) in (d). For the non-uniform moiré from (b), the triangle-wise distribution and the peak values directly from the FFT are not well aligned in (e). Both 2D histograms in (d) and (e) are weighted with respect to area fraction of individual triangles. Scale bars on real-space images are 1 μm, and scale bars on FFT images are 25 μm^{-1}.

distribution of the moiré domain walls. The phase and amplitude response are also sensitive to topography, so the presence of bubbles or wrinkles will dampen the phase or amplitude response and appear as large, dark regions.

Sample 1 (S1) with a small initial twist ($\theta \approx 0.111°$) annealed at 170°C shows a slight change to the domain size and isotropy between the as-fabricated sample in Fig. 3(b) and the same location in Fig. 3(c) after annealing for 30 s, but there is minimal change after continuous annealing for 30 min at 170°C [Fig. 3(d)], followed by annealing at 30 min at 400°C (shown in Fig. S1), and then for 30 min further at 600°C [Fig. 3(e)]. The region in which the moiré was measured in S1 was located next to a wrinkle, observable in Fig. 3(a), that relaxed within the first 30 s of annealing at 170°C (see Fig. S1). This may account for the minor but abrupt change in twist and strain ($\Delta\theta \approx 0.016°$, $\Delta\epsilon \approx 0.019\%$) following annealing for 30 s at 170°C relative to the pre-annealed state. However, there are negligible differences in the moiré between the geometry after 30 s at 170°C and that after 30 min at 170°C ($\Delta\theta \approx 0.006°$, $\Delta\epsilon \approx 0.001\%$) as well as 30 min at 600°C ($\Delta\theta \approx 0.001°$, $\Delta\epsilon \approx 0.001\%$). The entire series plotted in Fig. 3(k) suggests that continuous relaxation of twist and strain at these assembly-like conditions (170°C for 20–30 min) is unlikely for very small twist angles. Another sample with a similar initial twist, S2, exhibited negligible changes in twist and strain over 30 min at 170°C (see Figs. S2 and Fig. S3 in the supplementary material).

The sample with the larger initial twist angle, sample 3 (S3) ($\theta \approx 0.26°$), exhibited a more gradual decrease in twist while annealing at 400°C. The average moiré domain shown before annealing in Fig. 3(g) is enlarged after 15 min at 400°C in Fig. 3(h). The change in twist is a continuous process rather than an abrupt process as suggested by Fig. 3(k). Previous works have shown that hBN encapsulation suppresses out-of-plane corrugations and supports interfacial reconstruction,[18,35] which suggests that a larger number of hBN layers above the interface of interest should facilitate increased rotation as in-plane forces dominate. We observe that samples with smaller twist angles and with a thicker top layer of hBN (9–10 nm) did not significantly relax compared to a sample featuring a larger twist angle and with a thinner top hBN (3.3 nm). This suggests that the kinetics of the relaxation process are dominated by the contribution of the twist to the interfacial friction, which increases significantly at small twist angles approaching complete commensurability.[36]

Comparison between the topography of the sample before annealing and after 10 s annealing at 400°C [Fig. 3(h)] reveals significant lateral bubble migration, which is similar to S1. However, comparing the topography at 10 s and 1 h of annealing [Fig. 3(i)], the bubble movement is less evident. There is no moiré pattern evident in the bubbles seen in the phase maps in Figs. 3(e) and 3(f), which suggests that these bubbles are present at the interface between the flakes rather than at the interface between the bottom flake and

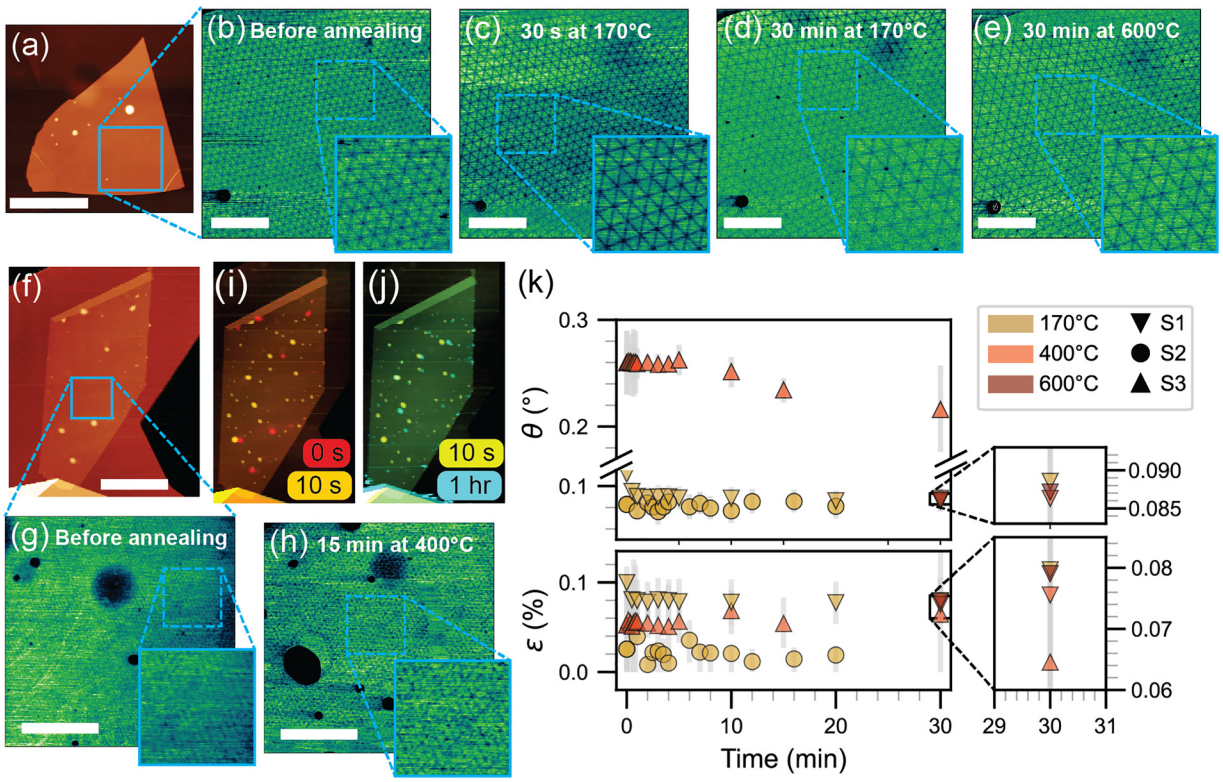

FIG. 3. Ferroelectric samples were annealed, and their moirés were measured at discrete intervals using AFM. The topography in (a) shows the measured area for sample 1 (S1) as well as the moiré before annealing (b) and after annealing for 30 s at 170°C in air (c), 30 min at 170°C in air (d), and 30 min at 600°C in Ar (e). Topography of sample 3 (S3) in (f) shows the measured area using CR-AFM before annealing (g) and after 15 min at 400°C in air (h). The topography channels after annealing S1 at 400°C were overlaid to show bubble migration between (i) 0 and 10 s as well as (j) 10 s and 1 h. Using the direct FFT method, the twist and strain for each sample are shown over time in (k). AFM topographical maps for the sample annealed at 400°C were overlaid to show bubble migration between (h) 0 and 10 s as well as (i) 10 s and 1 h. The twist and strain for S1 and S3 (using the direct FFT method) and S2 (using the real-space method) are shown in (k). Error bars are calculated as described in the supplementary material texts S2 and S3. Scale bars on images (a) and (f) are 5 μm and on images (b)–(e), (g), (h) are 1 μm.

underlying substrate and, therefore, may be more likely to influence the moiré relaxation behavior. In contrast, the measured twist angle of the sample relaxes on a different time scale, showing minimal change during the first few minutes followed by continuous modification during the subsequent 25 minutes, which is distinct from the abrupt change in S1. This suggests that bubble migration is not the sole factor in reconstruction during thermal annealing and that samples with larger initial twist values are more susceptible to continuous relaxation.

Time-dependent observations of annealed samples across a wider length scale [Fig. 4(a)] reveal that the evolution of thermal relaxation is strongly impacted by the local energy landscape. Substantial domain enlargement occurs between the as-assembled [Fig. 4(b)] and 8 h time point [Fig. 4(c)]. Continuing to anneal the sample in air at 400°C over several hours reveals two trends: a strong decrease and near-plateau in twist angle reduction, and a weak initial increase followed by a non-linear decrease in uniaxial strain highlighted in Fig. 4(f). The position closest to a large step shows an initial decrease in strain before increasing after a cumulative 2 h annealing period. There is also slightly more strain after 8 h annealing, which can be seen in comparing the anisotropy of the real-space moiré before annealing [Fig. 4(d)] and after 8 h at 400°C [Fig. 4(e)], though this effect is magnified due to the reduction in twist angle. For all regions, despite sometimes substantial changes to the strain within the first two hours of annealing, the final strain after 8 h only shows minor changes compared to the initial as-assembled strain. There does not appear to be a correlation between the magnitude of change in twist and magnitude of change in strain, though previous work shows that rotational reconstruction concentrates uniaxial strain at the domain walls.[35] It may be possible that the increase in strain is temporally correlated with twist angle relaxation, though further studies are necessary to confirm.

Contact between the relaxing top flake and the underlying bulk substrate affects relaxation behavior as well. A sample with a fairly large and non-uniform lattice, requiring the real-space extraction method, was annealed at 400°C in vacuum for several hours. The real-space vector mapping method was applied as there was a

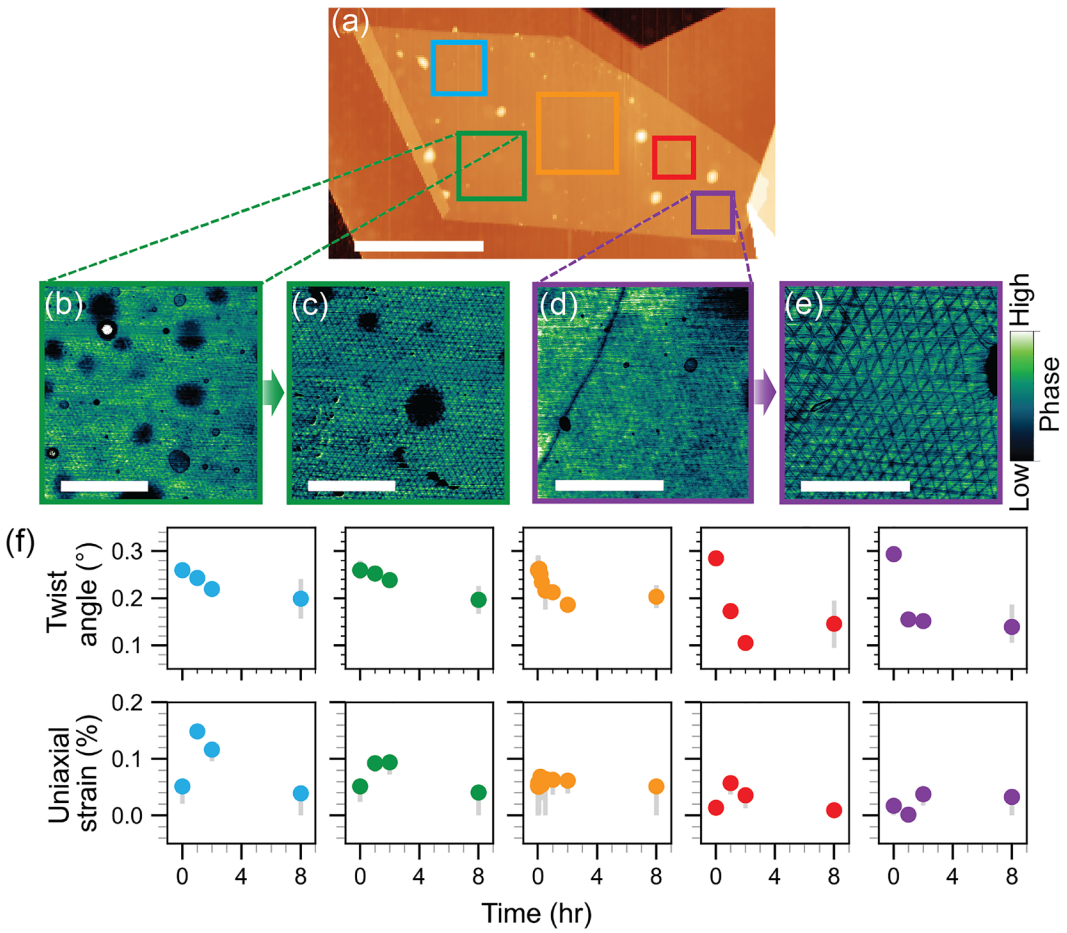

FIG. 4. Various positions around the sample were measured as indicated in topography of the as-assembled structure in (a). Representative CR-AFM phase channel images from one position (b) before annealing and (c) after 8 h shows a substantial increase in the moiré period. The real-space moiré from the position closest to the step edge of the flake (d) before annealing and (e) after 8 h shows a substantial increase in the unit cell size as well as a subtle increase in uniaxial strain compared to the pre-annealed sample. Local relaxation in twist and strain after annealing in air at 400°C is shown in (f) corresponding to the positions from the AFM topography in (a). Error bars were calculated as described in the supplementary material text S2. Scale bars are 5 μm in (a), 1 μm in (b), and (c), and 500 nm in (d) and (e).

large degree of inhomogeneity across the sample after assembly. The strain and twist can be measured for each half of the unit cell (i.e., each triangle), and the evolution in the distribution of the twist angle and strain can be examined. If the strain and twist for each discrete annealing step are plotted as a function of position within the sample as in Figs. 5(b)–5(c), there is a distinct gradient within the sample. When looking at the spatially averaged twist along the x axis in Fig. 5(f), it becomes clear that the interfacial twist is pinned in the regions closest to the silicon/hBN contact region. The spatially averaged strain along the x axis in Fig. 5(f) shows pinning within the center of the top flake and then variations toward both ends, though the end furthest from the silicon/hBN contact region shows the largest change. Similarly to the sample annealed in-air, the twist angle decreases in Fig. 5(d), and the uniaxial strain initially increases slightly, then decreases in Fig. 5(g). The width of the twist angle distribution is small before the anneal and broadens with 1 h of annealing, though it does not continue to increase. This suggests that annealing perturbs the uniformity of the interfacial twist, corroborating previous work on marginally twisted heterostructures,[21] though the amount of perturbation is not monotonic with the duration of annealing. While the width of the strain distribution does not change significantly over time, the width of the shear angle distribution in Fig. 5(h) increases. This implies that the uniformity of the strain directionality changes while the uniformity of the strain magnitude itself does not.

III. DISCUSSION

Thermal relaxation of moiré reconstructions can be challenging to untangle. Mechanisms governing a finite rate of relaxation are difficult to discern. In particular, strain has been shown to vary substantially across a small region even when interfacial twist does

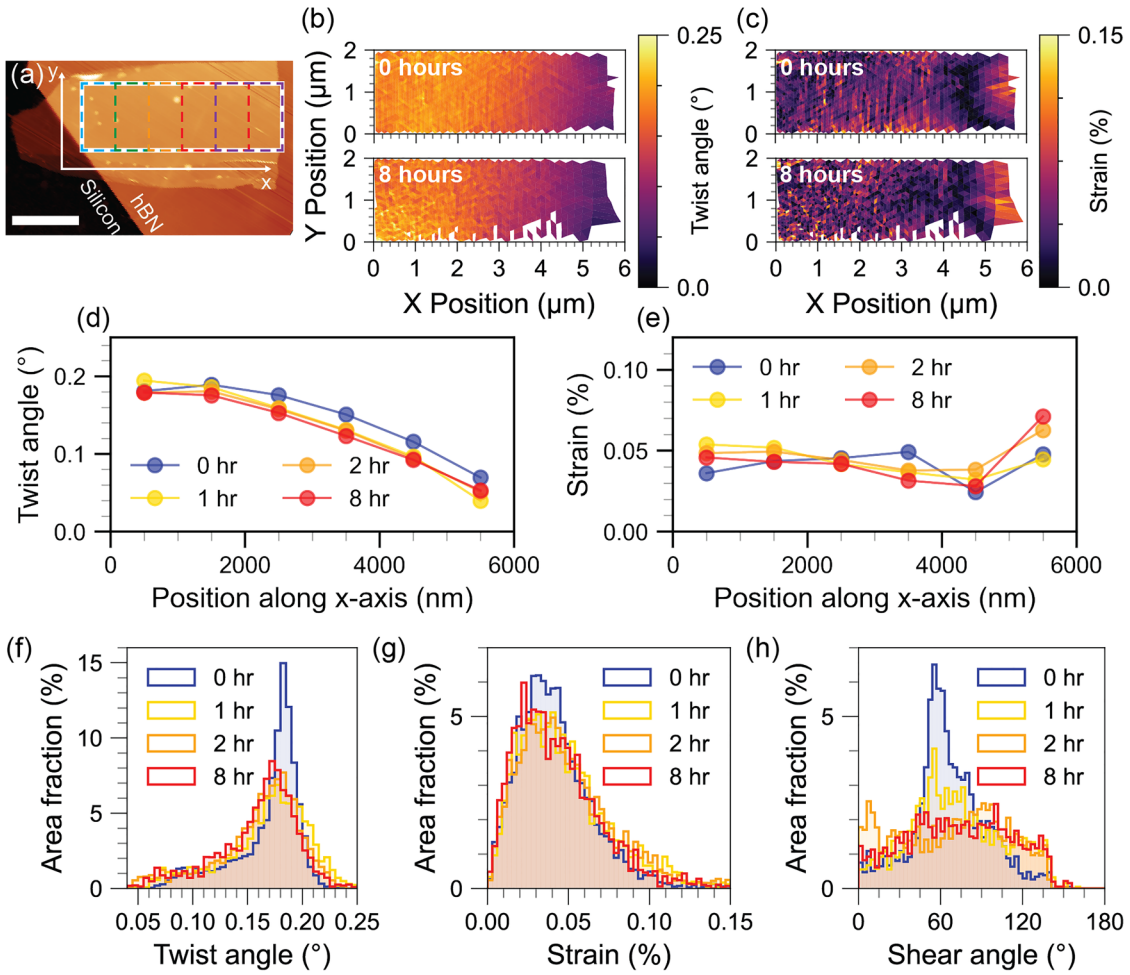

FIG. 5. (a) AFM topography of a sample annealed in vacuum ($p \leq 5 \times 10^{-6}$ Torr) at 400°C showing several overlapping positions where the superlattice was measured. The overlapping positions were stitched together to get a continuous map across the sample. The corresponding (b) twist and (c) strain maps for the as-assembled moiré and the annealed moiré are shown for each individual half-moiré unit cell. The spatially averaged twist and strain along the x axis are shown in in (d) and (e), respectively. The distributions of (f) twist, (g) strain, and (h) shear angle for the sample at several time points were extracted from these maps. Scale bars are 2 μm.

not vary substantially,[23,33] making its investigation and control even more significant. Our work has shown a reduction in twist angle that saturates at long annealing times as well as an increase in strain at short annealing times. Both parameters become less spatially uniform compared to the moiré before annealing. The driving force behind these trends is unclear.

Previous works suggest that thermal relaxation is primarily manifested through local atomic rearrangements rather than macroscopic flake rotation.[18,20] In encapsulated TMDC homobilayers, these rearrangements occur non-preferentially within both the top and bottom layer,[18] likely due to large lattice mismatch at the TMDC and hBN interfaces.[37] Non-encapsulated TMDC homobilayers show reduced or no further in-plane reconstructions at the same temperatures at which a fully encapsulated sample reaches complete commensuration,[18] presumably arising from competition with out-of-plane corrugations that are otherwise suppressed during encapsulation.[35] Local rearrangement may explain the minor absolute changes in strain before and after several hours of annealing seen in Fig. 4(f). However, macroscopic rotation of entire flakes after thermal annealing has also been observed optically in the case where the top layer is situated entirely on a thicker bottom flake without overhang onto a rough underlying substrate, shown in Fig. S3 as well as previous works.[14,21,22] This suggests that increased friction due to layer conformation with a rough substrate[38] is not negligible. It may explain the local fluctuations in strain seen in Fig. 5(e) as the atoms in the portion of the top flake furthest from the underlying substrate could more easily rearrange compared to the regions closer to contact with the silicon.

Other frictional effects must also be considered during thermal relaxation. In systems with small or nonexistent lattice mismatch, rotational friction peaks at commensurate states,[36] which would seemingly account for a plateau in twist angle reduction as

subsequently larger portions of the sample achieve commensuration through reconstruction. It may also account for decreased relaxation even at high temperatures for samples with a lower initial twist angle (see Fig. 3, Fig. S2, and Fig. S3). There is also evidence for a strain-dependent reduction in friction.[39] As the strain is reduced, the friction may increase as there is a lower energetic driving force for rearrangement, potentially contributing to the plateau in twist angle reduction. The relaxation rate during annealing was anticipated to be faster because the coefficient of friction between two interfaces is reduced in vacuum as there are fewer adsorbates.[40,41] While this suggests that other frictional effects may be dominating, it also offers an opportunity for future works to study the effect of annealing environment on assembled heterostructures.

Metastable rotational states may also contribute to a relaxation plateau. Theory indicates that there is a local energetic minima for parallel-stacked AB/BA domains near zero interfacial twist, and this local minima shifts closer to zero as the size of the flake increases.[42,43] Experimental work with graphene/hBN supports this with a metastable state close to 0.7°,[21] though the effect is not consistent, and it has not been shown in homobilayers. Further work suggests that heterostrain can stabilize the interfacial twist above zero even at elevated temperatures,[44] providing another factor that may contribute to a metastable state.

Differences in relaxation rates may be partially attributed to interfacial contamination. Trapped water or alcohol molecules have been shown to increase the interfacial friction, and the increase scales proportionally with the amount of solvent.[45,46] Previous work shows that significant rotation does not always occur in heterostructures, particularly those with large amounts of bubbles or other interlayer contaminants.[21,22] This suggests that twist angle reduction in heterostructures with larger amounts of interfacial contamination would plateau earlier than in clean heterostructures and offers an opportunity for further investigation of relaxation rate with respect to sample cleanliness.

IV. CONCLUSIONS

We have shown evidence of a finite, non-linear twist and strain relaxation rate in parallel-stacked hBN structures through thermal annealing. Successive annealing steps reduce the interfacial twist to a saturation point as well as reducing twist uniformity. Uniaxial heterostrain tends toward an initial increase at short annealing times and then decreases after further annealing, though its directionality decreases in uniformity. However, through considerations during assembly, it is possible to exploit pinning points to create an intentional and directional gradient in twist and strain without mechanical interference. This work provides a greater understanding of the effect of annealing on near-zero moiré superlattices and other steps toward controlling moiré geometry after fabrication.

SUPPLEMENTARY MATERIAL

See the supplementary material for detailed methods, further AFM scans of samples S1–S3, and optical images of hBN/hBN samples showing macroscopic rotation after annealing in air at 400°C. A separate video taken using a FLIR ONE camera shows a silicon chip being placed on to a 400°C hotplate to demonstrate the time necessary for the chip to reach the appropriate temperature.

ACKNOWLEDGMENTS

The authors thank Chaitrali Duse and Marc Kastner for fruitful discussions. Annealing procedures and moiré measurements were supported by the U.S. Department of Energy, Office of Science, Basic Energy Sciences, Materials Sciences and Engineering Division, under Contract No. DE-AC02-76SF00515. Development of tools for robotic stacking of 2D materials was supported by SLAC National Accelerator Laboratory under the Q-BALMS Laboratory Directed Research and Development funds. Initial development of twisted hBN fabrication protocols was supported by the U.S. Department of Energy (DOE) Basic Energy Sciences Grant No. DE-SC0021984. The process for fabricating polymeric stamps was supported by the National Science Foundation (No. DMR-2018008). Part of this work was performed at the Stanford Nano Shared Facilities (SNSF), supported by the National Science Foundation under Award No. ECCS-2026822, as well as in the nano@Stanford labs, which are supported by the National Science Foundation as part of the National Nanotechnology Coordinated Infrastructure under Award No.ECCS-1542152. M.H. acknowledges partial support from the U.S. Department of Defense through the Graduate Fellowship in STEM Diversity program. K.W. and T.T. acknowledge support from the JSPS KAKENHI (Grant Nos. 21H05233 and 23H02052) and World Premier International Research Center Initiative (WPI), MEXT, Japan.

AUTHOR DECLARATIONS

Conflict of Interest

The authors have no conflicts to disclose.

Author Contributions

Marisa Hocking: Conceptualization (equal); Formal analysis (equal); Investigation (equal); Software (equal); Visualization (equal); Writing – original draft (equal); Writing – review & editing (equal). **Christina E. Henzinger:** Formal analysis (supporting). **Steven J. Tran:** Resources (equal). **Mihir Pendharkar:** Resources (equal). **Nathan J. Bittner:** Resources (equal). **Kenji Watanabe:** Resources (equal). **Takashi Taniguchi:** Resources (equal). **David Goldhaber-Gordon:** Funding acquisition (equal); Supervision (equal); Writing – review & editing (equal). **Andrew J. Mannix:** Conceptualization (equal); Funding acquisition (equal); Supervision (equal); Writing – original draft (equal); Writing – review & editing (equal).

DATA AVAILABILITY

The data that support the findings of this study are available from the corresponding author upon reasonable request.

REFERENCES

[1]Y. Cao, V. Fatemi, S. Fang, K. Watanabe, T. Taniguchi, E. Kaxiras, and P. Jarillo-Herrero, Nature **556**, 43 (2018).

[2]A. L. Sharpe, E. J. Fox, A. W. Barnard, J. Finney, K. Watanabe, T. Taniguchi, M. A. Kastner, and D. Goldhaber-Gordon, Science **365**, 605 (2019).
[3]E. C. Regan, D. Wang, C. Jin, M. I. Bakti Utama, B. Gao, X. Wei, S. Zhao, W. Zhao, Z. Zhang, K. Yumigeta, M. Blei, J. D. Carlström, K. Watanabe, T. Taniguchi, S. Tongay, M. Crommie, A. Zettl, and F. Wang, Nature **579**, 359 (2020).
[4]K. Ko, A. Yuk, R. Engelke, S. Carr, J. Kim, D. Park, H. Heo, H.-M. Kim, S.-G. Kim, H. Kim, T. Taniguchi, K. Watanabe, H. Park, E. Kaxiras, S. M. Yang, P. Kim, and H. Yoo, Nat. Mater. **22**, 992–998 (2023).
[5]S. Deb, W. Cao, N. Raab, K. Watanabe, T. Taniguchi, M. Goldstein, L. Kronik, M. Urbakh, O. Hod, and M. Ben Shalom, Nature **612**, 465–469 (2022).
[6]A. Weston, E. G. Castanon, V. Enaldiev, F. Ferreira, S. Bhattacharjee, S. Xu, H. Corte-León, Z. Wu, N. Clark, A. Summerfield, T. Hashimoto, Y. Gao, W. Wang, M. Hamer, H. Read, L. Fumagalli, A. V. Kretinin, S. J. Haigh, O. Kazakova, A. K. Geim, V. I. Fal'ko, and R. Gorbachev, Nat. Nanotechnol. **17**, 390 (2022).
[7]C. R. Woods, P. Ares, H. Nevison-Andrews, M. J. Holwill, R. Fabregas, F. Guinea, A. K. Geim, K. S. Novoselov, N. R. Walet, and L. Fumagalli, Nat. Commun. **12**, 347 (2021).
[8]K. Yasuda, X. Wang, K. Watanabe, T. Taniguchi, and P. Jarillo-Herrero, Science **372**, 1458–1462 (2021).
[9]M. Vizner Stern, Y. Waschitz, W. Cao, I. Nevo, K. Watanabe, T. Taniguchi, E. Sela, M. Urbakh, O. Hod, and M. Ben Shalom, Science **372**, 1462–1466 (2021).
[10]J. Fraunié, R. Jamil, R. Kantelberg, S. Roux, L. Petit, E. Lepleux, L. Pacheco, K. Watanabe, T. Taniguchi, V. Jacques, L. Lombez, M. M. Glazov, B. Lassagne, X. Marie, and C. Robert, Phys. Rev. Mater. **7**, L121002 (2023).
[11]D. S. Kim, R. C. Dominguez, R. Mayorga-Luna, D. Ye, J. Embley, T. Tan, Y. Ni, Z. Liu, M. Ford, F. Y. Gao, S. Arash, K. Watanabe, T. Taniguchi, S. Kim, C.-K. Shih, K. Lai, W. Yao, L. Yang, X. Li, and Y. Miyahara, Nat. Mater. **23**, 65–70 (2024).
[12]Y. Yang, J. Li, J. Yin, S. Xu, C. Mullan, T. Taniguchi, K. Watanabe, A. K. Geim, K. S. Novoselov, and A. Mishchenko, Sci Adv **6**, 0 (2020).
[13]L. Du, H. Yu, M. Liao, S. Wang, L. Xie, X. Lu, J. Zhu, N. Li, C. Shen, P. Chen, R. Yang, D. Shi, and G. Zhang, Appl. Phys. Lett. **111**, 263106 (2017).
[14]D. Wang, G. Chen, C. Li, M. Cheng, W. Yang, S. Wu, G. Xie, J. Zhang, J. Zhao, X. Lu, P. Chen, G. Wang, J. Meng, J. Tang, R. Yang, C. He, D. Liu, D. Shi, K. Watanabe, T. Taniguchi, J. Feng, Y. Zhang, and G. Zhang, Phys. Rev. Lett. **116**, 126101 (2016).
[15]R. Ribeiro-Palau, C. Zhang, K. Watanabe, T. Taniguchi, J. Hone, and C. R. Dean, Science **361**, 690 (2018).
[16]M. Kapfer, B. S. Jessen, M. E. Eisele, M. Fu, D. R. Danielsen, T. P. Darlington, S. L. Moore, N. R. Finney, A. Marchese, V. Hsieh, P. Majchrzak, Z. Jiang, D. Biswas, P. Dudin, J. Avila, K. Watanabe, T. Taniguchi, S. Ulstrup, P. Bøggild, P. J. Schuck, D. N. Basov, J. Hone, and C. R. Dean, Science **381**, 677 (2023).
[17]M. Souibgui, H. Ajlani, A. Cavanna, M. Oueslati, A. Meftah, and A. Madouri, Superlattices Microstruct. **112**, 394 (2017).
[18]J.-H. Baek, H. G. Kim, S. Y. Lim, S. C. Hong, Y. Chang, H. Ryu, Y. Jung, H. Jang, J. Kim, Y. Zhang, K. Watanabe, T. Taniguchi, P. Y. Huang, H. Cheong, M. Kim, and G.-H. Lee, Nat. Mater. **1**, 1463–1469 (2023).
[19]Z. Zhu, L. Zhan, T.-M. Shih, W. Wan, J. Lu, J. Huang, S. Guo, Y. Zhou, and W. Cai, Small **14**, e1802498 (2018).
[20]J. S. Alden, A. W. Tsen, P. Y. Huang, R. Hovden, L. Brown, J. Park, D. A. Muller, and P. L. McEuen, Proc. Natl. Acad. Sci. U.S.A. **110**, 11256 (2013).
[21]C. R. Woods, F. Withers, M. J. Zhu, Y. Cao, G. Yu, A. Kozikov, M. Ben Shalom, S. V. Morozov, M. M. van Wijk, A. Fasolino, M. I. Katsnelson, K. Watanabe, T. Taniguchi, A. K. Geim, A. Mishchenko, and K. S. Novoselov, Nat. Commun. **7**, 10800 (2016).
[22]L. Wang, Y. Gao, B. Wen, Z. Han, T. Taniguchi, K. Watanabe, M. Koshino, J. Hone, and C. R. Dean, Science **350**, 1231 (2015).
[23]T. A. de Jong, T. Benschop, X. Chen, E. E. Krasovskii, M. J. A. de Dood, R. M. Tromp, M. P. Allan, and S. J. van der Molen, Nat. Commun. **13**, 70 (2022).
[24]M. Zhu, D. Ghazaryan, S.-K. Son, C. R. Woods, A. Misra, L. He, T. Taniguchi, K. Watanabe, K. S. Novoselov, Y. Cao, and A. Mishchenko, 2D Mater. **4**, 011013 (2016).
[25]D. A. Cosma, J. R. Wallbank, V. Cheianov, and V. I. Fal'ko, Faraday Discuss. **173**, 137 (2014).
[26]Y. Bai, L. Zhou, J. Wang, W. Wu, L. J. McGilly, D. Halbertal, C. F. B. Lo, F. Liu, J. Ardelean, P. Rivera, N. R. Finney, X.-C. Yang, D. N. Basov, W. Yao, X. Xu, J. Hone, A. N. Pasupathy, and X.-Y. Zhu, Nat. Mater. **19**, 1068 (2020).
[27]C. Ma, Y. Chen, W. Arnold, and J. Chu, J. Appl. Phys. **121**, 154301 (2017).
[28]M. H. van Es, A. Mohtashami, R. M. T. Thijssen, D. Piras, P. L. M. J. van Neer, and H. Sadeghian, Ultramicroscopy **184**, 209 (2018).
[29]C. R. Woods, L. Britnell, A. Eckmann, R. S. Ma, J. C. Lu, H. M. Guo, X. Lin, G. L. Yu, Y. Cao, R. V. Gorbachev, A. V. Kretinin, J. Park, L. A. Ponomarenko, M. I. Katsnelson, Y. N. Gornostyrev, K. Watanabe, T. Taniguchi, C. Casiraghi, H.-J. Gao, A. K. Geim, and K. S. Novoselov, Nat. Phys. **10**, 451 (2014).
[30]J. Tamayo and R. García, Appl. Phys. Lett. **71**, 2394 (1997).
[31]X. Wang, J. Finney, A. L. Sharpe, L. K. Rodenbach, C. L. Hsueh, K. Watanabe, T. Taniguchi, M. A. Kastner, O. Vafek, and D. Goldhaber-Gordon, Proc. Natl. Acad. Sci. U.S.A. **120**, e2307151120 (2023).
[32]Q. Peng, W. Ji, and S. De, Comput. Mater. Sci. **56**, 11 (2012).
[33]N. P. Kazmierczak, M. Van Winkle, C. Ophus, K. C. Bustillo, S. Carr, H. G. Brown, J. Ciston, T. Taniguchi, K. Watanabe, and D. K. Bediako, Nat. Mater. **20**, 956 (2021).
[34]R. Engelke, H. Yoo, S. Carr, K. Xu, P. Cazeaux, R. Allen, A. M. Valdivia, M. Luskin, E. Kaxiras, M. Kim, J. H. Han, and P. Kim, Phys. Rev. B Condens. Matter **107**, 125413 (2023).
[35]M. Van Winkle, I. M. Craig, S. Carr, M. Dandu, K. C. Bustillo, J. Ciston, C. Ophus, T. Taniguchi, K. Watanabe, A. Raja, S. M. Griffin, and D. K. Bediako, Nat. Commun. **14**, 2989 (2023).
[36]M. Dienwiebel, G. S. Verhoeven, N. Pradeep, J. W. M. Frenken, J. A. Heimberg, and H. W. Zandbergen, Phys. Rev. Lett. **92**, 126101 (2004).
[37]M. Liao, P. Nicolini, L. Du, J. Yuan, S. Wang, H. Yu, J. Tang, P. Cheng, K. Watanabe, T. Taniguchi, L. Gu, V. E. P. Claerbout, A. Silva, D. Kramer, T. Polcar, R. Yang, D. Shi, and G. Zhang, Nat. Mater. **21**, 47 (2022).
[38]Y. Dong, J. Phys. D Appl. Phys. **47**, 055305 (2014).
[39]S. Zhang, Y. Hou, S. Li, L. Liu, Z. Zhang, X.-Q. Feng, and Q. Li, Proc. Natl. Acad. Sci. U. S. A. **116**, 24452 (2019).
[40]J. M. Martin, C. Donnet, T. Le Mogne, and T. Epicier, Phys. Rev. B Condens. Matter **48**, 10583 (1993).
[41]G. He, M. H. Muser, and M. O. Robbins, Science **284**, 1650 (1999).
[42]S. Zhu, P. Pochet, and H. T. Johnson, ACS Nano **13**, 6925 (2019).
[43]S. Bagchi, H. T. Johnson, and H. B. Chew, Phys. Rev. B Condens. Matter **101**, 054109 (2020).
[44]X. Yang and B. Zhang, Sci. Rep. **13**, 4364 (2023).
[45]H. Lee, J.-H. Ko, J. S. Choi, J. H. Hwang, Y.-H. Kim, M. Salmeron, and J. Y. Park, J. Phys. Chem. Lett. **8**, 3482 (2017).
[46]E. Dollekamp, P. Bampoulis, M. H. Siekman, E. S. Kooij, and H. J. W. Zandvliet, Langmuir **35**, 4886 (2019).